

# Assembly and Photocarrier Dynamics of Heterostructured Nanocomposite Photoanodes from Multicomponent Colloidal Nanocrystals

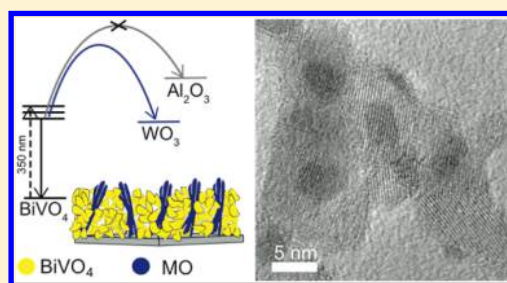
Anna Loiudice,<sup>†,‡</sup> Jason K. Cooper,<sup>†,‡</sup> Lucas H. Hess,<sup>†,‡</sup> Tracy M. Mattox,<sup>§</sup> Ian D. Sharp,<sup>\*,†,||</sup> and R. Buonsanti<sup>\*,†,‡</sup>

<sup>†</sup>Joint Center for Artificial Photosynthesis, <sup>‡</sup>Materials Science Division, <sup>§</sup>The Molecular Foundry, and <sup>||</sup>Chemical Sciences Division, Lawrence Berkeley National Laboratory, One Cyclotron Road, Berkeley, California 94720, United States

## Supporting Information

**ABSTRACT:** Multicomponent oxides and their heterostructures are rapidly emerging as promising light absorbers to drive oxidative chemistry. To fully exploit their functionality, precise tuning of their composition and structure is crucial. Here, we report a novel solution-based route to nanostructured bismuth vanadate ( $\text{BiVO}_4$ ) that facilitates the assembly of  $\text{BiVO}_4$ /metal oxide ( $\text{TiO}_2$ ,  $\text{WO}_3$ , and  $\text{Al}_2\text{O}_3$ ) nanocomposites in which the morphology of the metal oxide building blocks is finely tailored. The combination of transient absorption spectroscopy—spanning from picoseconds to second time scales—and photoelectrochemical measurements reveals that the achieved structural tunability is key to understanding and directing charge separation, transport, and efficiency in these complex oxide heterostructured films.

**KEYWORDS:** Colloidal synthesis, ternary oxides, assembly, photoelectrochemistry, charge dynamics



Achieving fine control over the composition and stoichiometry of multicomponent oxide materials is a nontrivial, yet technologically important, challenge that has significant implications for a number of applications, including batteries, smart windows, fuel cells, and resistive switching memories.<sup>1–4</sup> In the context of solar-to-chemical energy conversion, complex oxides are receiving increasing attention as photocatalysts to drive oxidative chemical reactions, and in particular water oxidation, since they exhibit relatively high stability under oxidative and corrosive conditions.<sup>5,6</sup> Oxides containing  $d^0$  (e.g.,  $\text{Ti(IV)}$ ,  $\text{V(V)}$ ,  $\text{W(VI)}$ ) and  $s^2$  (e.g.,  $\text{Sn(II)}$ ,  $\text{Bi(III)}$ ,  $\text{Sb(III)}$ ) elements have resulted in a class of promising visible light absorbing photoanodes, including the well-studied  $\text{BiVO}_4$  and less explored systems such as  $\text{Bi}_2\text{WO}_6$ ,  $\text{SnWO}_4$ , and  $\text{SnNb}_2\text{O}_6$ .<sup>7–12</sup> However, the performance criteria for photoanodes are complex and difficult to meet in any one material. Hence, heterojunction architectures have been developed to take advantage of favorable properties of two different oxide materials, while also overcoming their deficiencies. Specifically, smaller band gap materials, such as  $\text{Fe}_2\text{O}_3$  or  $\text{BiVO}_4$ , exhibit increased light absorption in the visible spectrum, but their performance losses are generally attributed to a short photocarrier lifetime ( $\text{Fe}_2\text{O}_3$ ) and limited photoexcited electron mobility and conductivity ( $\text{Fe}_2\text{O}_3$  and  $\text{BiVO}_4$ ).<sup>13–22</sup> Meanwhile, larger band gap metal oxides (MO), such as  $\text{TiO}_2$ ,  $\text{ZnO}$ , or  $\text{WO}_3$ , may have improved mobility but reduced visible light absorption. Therefore, combining smaller band gap and larger band gap metal oxides in heterostructures (i.e.,  $\text{Fe}_2\text{O}_3/\text{WO}_3$ ,  $\text{BiVO}_4/\text{TiO}_2$ ,  $\text{BiVO}_4/\text{WO}_3$ ) has been shown to enhance the

water oxidation photocurrent.<sup>13–22</sup> To cite one of the most recent examples, Shi et al. have demonstrated that W, Mo-codoped  $\text{BiVO}_4$ -decorated  $\text{WO}_3$  helical nanostructures exhibit among the highest photocurrent densities to date for  $\text{BiVO}_4$ -based photoanodes, specifically  $5.35 \text{ mA/cm}^2$  at the reversible water oxidation potential of 1.23 V versus reversible hydrogen electrode (RHE), after catalyst deposition.<sup>21</sup> This enhancement was attributed to a combination of effective light scattering, improved charge separation and transport, and an enlarged interfacial contact area with the electrolyte.

The performance enhancements achieved in oxide heterostructures are not only strongly dependent on light absorber composition, but also on structural parameters, such as characteristic size, shape, and the relative arrangement of the two components.<sup>13–27</sup> Opposing structural modifications are often required to improve one parameter at the cost of another. For example, a large interfacial area at the heterojunction, obtained by nanostructuring, is advantageous for charge separation but can be detrimental for charge transport, which would benefit from a more extended crystalline network.<sup>13–27</sup> When aiming at maximizing photoelectrochemical (PEC) performance, the ability to tailor-make material platforms with tunable morphological characteristics in an unrestricted compositional range is critical for achieving optimal design specifications, as well as for providing understanding of the sensitivities of performance parameters to different composi-

Received: July 7, 2015

Published: October 12, 2015

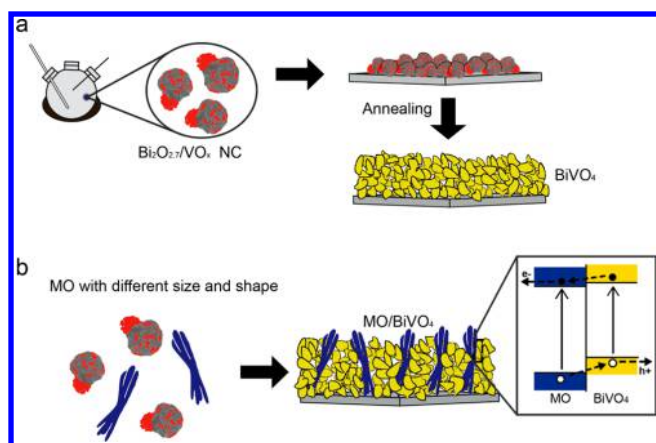
tional and structural parameters. Although they have led to significant advances in the field, the previously reported systems do not yet possess the broad synthetic tunability required to systematically probe the important roles of structure and composition on photocarrier transport in multicomponent oxide heterostructures.

Our approach to gain structural and compositional control is to synthesize and assemble colloidal nanocrystals (NCs), a strategy that has been fruitful in recent years for addressing similar scientific needs in other technological areas.<sup>28–33</sup> The superior control afforded by colloidal chemistry, including composition, size, and shape, combined with solution processability and rich surface chemistry, has provided access to modular inorganic nanocomposites with an unprecedented tunability.<sup>2,28–33</sup> Nonetheless, the full potential of colloidal chemistry has not yet been explored to construct complex functional 3D architectures for solar-to-chemical energy conversion.

One of the hurdles to realizing oxide heterojunctions suitable for PEC with tailored structure and composition by NC assembly is the lack of colloidal approaches for the synthesis of ternary and quaternary oxide light absorbers. While well-established colloidal routes exist for complex multielement chalcogenides (e.g., CuZnSSe, PbSeSe, PbSeTe), which have been widely used for ink-based photovoltaics, the synthesis of ternary and quaternary oxide NCs still remains to be fully explored.<sup>34–38</sup>

In this work, first a colloidal synthetic strategy to access monoclinic BiVO<sub>4</sub> nanostructured thin film photoanodes is described. Specifically, Bi<sub>2</sub>O<sub>2.7</sub>/VO<sub>x</sub> NC heterodimers were synthesized, and their thermal evolution into BiVO<sub>4</sub> films was followed by X-ray diffraction and optical spectroscopy. Second, the heterodimers were assembled with presynthesized TiO<sub>2</sub>, WO<sub>3</sub>, and Al<sub>2</sub>O<sub>3</sub> NCs with different sizes and shapes to fabricate heterostructured nanocomposites, achieving unprecedented structural tunability compared with previous work (Scheme 1).<sup>13–22</sup> Due to the favorable energetics for selective extraction of photoexcited electrons from BiVO<sub>4</sub> to WO<sub>3</sub>, the impact of the nanostructure on PEC performance, as well as photocarrier separation, recombination, and extraction, was specifically investigated for the case of BiVO<sub>4</sub>/WO<sub>3</sub> nanocomposite heterostructures.

### Scheme 1. Schematic Representation of the Novel Colloidal-Based Approach to MO Heterostructured Photoanodes Developed in This Work



### Synthesis of Bi<sub>2</sub>O<sub>2.7</sub>/VO<sub>x</sub> NC Heterodimers and Their Thermal Evolution into Nanostructured BiVO<sub>4</sub> Films.

Organic-capped Bi<sub>2</sub>O<sub>2.7</sub>/VO<sub>x</sub> NC heterodimers were synthesized through an in situ seed-mediated growth, where Bi nanosheets generated in the reaction flask (see Figure S1) act as seeds for the nucleation of a noncentrosymmetric vanadium oxide shell. Bismuth chloride (BiCl<sub>3</sub>) was used as a bismuth precursor and vanadyl acetylacetonate (VO(acac)<sub>2</sub>) as a vanadium source, while oleylamine was used as surfactant and solvent (see SI for experimental details). BiCl<sub>3</sub> was reduced to elemental bismuth in the form of nanosheets by the amine. After reaction of the Bi nanosheets with VO(acac)<sub>2</sub>, Bi<sub>2</sub>O<sub>2.7</sub>/VO<sub>x</sub> NC heterodimers were precipitated and redispersed in hexane. Similar results, with a lower product yield, were obtained when the bismuth and vanadium precursors were introduced simultaneously at the beginning of the synthesis (Figure S2). Transmission electron microscopy (TEM) and high-angle annular dark field scanning TEM (HAADF-STEM) images at different magnification (Figure 1a,b and insets)

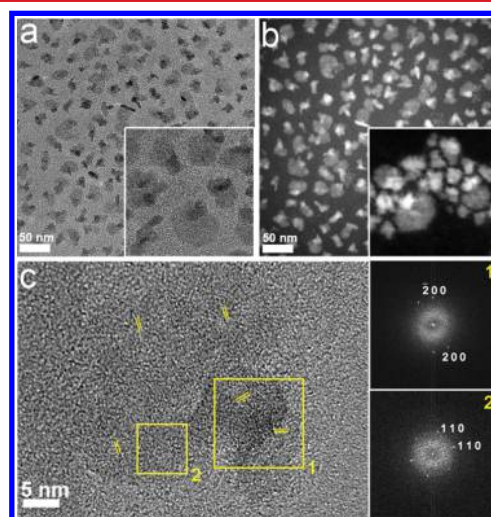


**Figure 1.** (a) Low-resolution TEM and (b) STEM-HAADF images of as-synthesized Bi<sub>2</sub>O<sub>2.7</sub>/VO<sub>x</sub> NC heterodimers; (c) HRTEM image of a single heterodimer, along with the FFTs from the corresponding regions enclosed by labeled yellow boxes (right).

showed uniformly dispersed NCs, with an average size of  $25 \pm 4$  nm, comprised of two domains arranged in a nonconcentric dimer-like topology. High-resolution TEM (HRTEM) analysis (Figure 1c) elucidated the nature of the two differently contrasted regions in the heterodimers. As shown in Figure 1c, the darker domain is fully crystalline while the lower contrast domain is composed of smaller crystalline domains embedded in an amorphous matrix. The *d*-spacing of the lattice fringes in the crystalline domain, as derived from fast Fourier transform (FFT) analysis (insets in Figure 1c), were equal to  $d = 2.0$  Å and  $d = 2.6$  Å, which correspond closely to the (2 0 0) [ $d_{200} = 1.9$  Å] and (1 1 0) [ $d_{110} = 2.7$  Å] planes of the Bi<sub>2</sub>O<sub>2.7</sub> tetragonal crystal structure (PDF No. 30-065-4028). STEM-energy dispersive X-ray spectroscopy (EDS) analysis on single NCs revealed the presence of both bismuth and vanadium within the NC heterodimers (see Figure S3).

The existence of crystalline domains of Bi<sub>2</sub>O<sub>2.7</sub> in the heterodimers was confirmed also by X-ray diffraction (XRD) analysis. The XRD pattern of the as-deposited NCs (Figure 2a, black line) showed two broad peaks at  $2\theta = 32.9^\circ$  and  $47.1^\circ$ ,

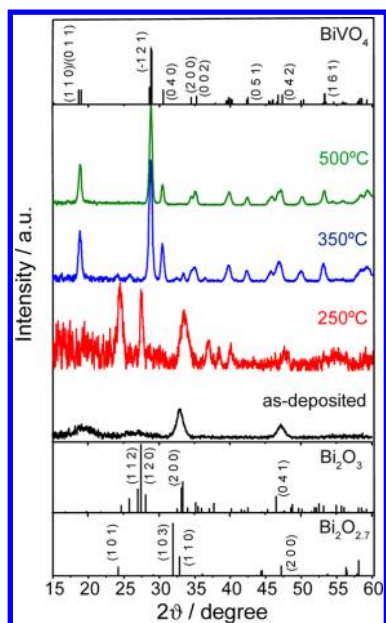


**Figure 2.** XRD patterns of the NC film as-deposited (black line), annealed at 250 °C for 2 h (red line), at 350 °C for 2 h (blue line), and at 500 °C for 10 min (green line).

ascribable to the  $\text{Bi}_2\text{O}_{2.7}$  tetragonal crystal structure (JCPDS No. 03-065-4028). Scherrer analysis performed on the peak at  $2\theta = 47.1^\circ$  revealed an average crystallite size of  $\sim 10$  nm, consistent with the size of the fully crystalline domains observed in the TEM images. Structural refinement through Rietveld analysis was hindered by the low intensity and broadness of the XRD peaks. Therefore, positive identification of the broad hump at lower  $2\theta$  was not possible.

Inductively coupled plasma optical emission spectroscopy (ICP-OES) analysis revealed that the NC heterodimers contained bismuth and vanadium with a molar ratio Bi:V of 1:1.4, corresponding to a vanadium-rich composition. X-ray photoelectron spectroscopy (XPS) analysis yielded the same Bi to V molar ratio and an oxidation state of +3 and +5 for bismuth and vanadium, respectively (Figure S4 a,b). While both HRTEM and XRD identified  $\text{Bi}_2\text{O}_{2.7}$  as the main phase in the crystalline domains, the combination of ICP, XPS, and STEM-EDS results suggests that the composition of the lower contrast domains in the TEM images likely corresponds to vanadium oxide ( $\text{VO}_x$ ) or to a Bi–V–O compound. This hypothesis of formation of amorphous  $\text{VO}_x$  or Bi–V–O nanosize domains is consistent with previous reports.<sup>39,40</sup> The existence of many stable  $\text{VO}_x$  polymorphs and of additional metastable phases, especially at the nanoscale, accounts for the difficulty to crystallize  $\text{VO}_x$  nanoparticles or to identify their structure when crystalline.<sup>40</sup> With regard to the Bi–V–O compound, Choi et al. assigned their poorly crystalline films to  $\text{Bi}_4\text{V}_6\text{O}_{21}$ , one stable phase in the Bi–V–O family composed of Bi(III) and V(V); however, we cannot definitively confirm or exclude its presence in our system.<sup>8</sup>

To form functional semiconductor thin films, the as-synthesized  $\text{Bi}_2\text{O}_{2.7}/\text{VO}_x$  NC heterodimers were spin-coated on silicon substrates and annealed at different temperatures, and the resulting changes in crystal structure were recorded by XRD. As shown in Figure 2, after annealing at 250 °C for 2 h in air, new peaks at  $2\theta = 24.2^\circ, 27.3^\circ, 36.3^\circ, 37.1^\circ,$  and  $39.5^\circ$  appeared with respect to the as-deposited sample. Most of these

new peaks were in good accordance with the XRD pattern of monoclinic  $\text{Bi}_2\text{O}_3$  (JCPDS No. 04-005-4873), suggesting that during the annealing step at 250 °C, oxygen is incorporated in the tetragonal nonstoichiometric  $\text{Bi}_2\text{O}_{2.7}$  lattice (JCPDS No. 30-065-4028). As the annealing temperature was increased to 350 °C, the film crystallized into the monoclinic  $\text{BiVO}_4$  phase, as evidenced by the appearance of intense peaks at  $2\theta = 29^\circ, 31^\circ$ . However, an impurity phase was still present (i.e.,  $2\theta = 33^\circ$ ), suggesting that a higher temperature is required to complete the transformation. After annealing for 10 min at 500 °C in air, the film crystallized into pure monoclinic  $\text{BiVO}_4$  phase (JCPDS No. 00-014-0688), and the narrowing of the peaks indicated an increase of the film grain size up to  $\sim 80$  nm ( $\sim 30$  nm for the films annealed at 350 °C) that is evident also in the SEM images (Figure S5). XPS and Raman spectroscopy data were also consistent with the assigned annealing-induced phase transformations (Figure S4). The importance of the presence of Bi, V, and O within the same NC building blocks was evidenced by the failure to obtain monoclinic  $\text{BiVO}_4$  films when separately synthesized and purified Bi NCs were reacted with the vanadium precursor (Figure S6).

It is important to note that, although XRD analysis for the discussed reaction conditions indicated the presence of the pure  $\text{BiVO}_4$  phase in samples annealed at 500 °C, Raman spectroscopy revealed that amorphous  $\text{V}_2\text{O}_5$  is also present (Figure S4c). This finding was not surprising considering the vanadium-rich composition of the heterodimers measured by ICP-OES analysis. For samples prepared with a lower concentration of the bismuth precursor in the reaction mixture,  $\text{V}_2\text{O}_5$  was clearly detected by XRD after annealing (Figure S7). With higher concentration of bismuth precursor, a major fraction of the sample was instead composed of 300 nm Bi spheres (Figure S8). As previously reported, immersing the films in 1 M NaOH solution for 30 s was sufficient to selectively remove  $\text{V}_2\text{O}_5$  (see Table S1).<sup>7</sup> The phase transformation  $\text{Bi}_2\text{O}_{2.7}/\text{VO}_x \rightarrow \text{Bi}_2\text{O}_3/\text{VO}_x \rightarrow \text{BiVO}_4$  was also monitored by UV–vis absorption spectroscopy (see Figure S9 and S10), and the data were consistent with the results obtained by XRD.

Transient absorption (TA) spectroscopy was utilized to study the excited state dynamics of the nanostructured  $\text{BiVO}_4$  films as a function of sample annealing temperatures of 350 and 500 °C. Long-lived photoexcited charge carriers are often associated with enhanced PEC performance of photoelectrodes. Longer photocarrier lifetimes generally correspond to reduced recombination rates, which compete directly with charge transfer to drive the desired redox reaction, such as water oxidation in the present case.<sup>41–43</sup> TA measurements offer an opportunity to examine the role of carrier surface trapping, expected due to the nanostructured nature of the material, and crystallinity on the excited state lifetime. The time dependence of the normalized transient differential absorption (dA) recovery, and the results of multiexponential fitting analysis are shown in Figure 3. For the 350 °C (500 °C) annealed sample, the extracted lifetimes were 1.4, 7.0, and 40 ns (2.7, 11, and 100 ns). Henceforth, these three components will be referred to as “fast”, “medium”, and “slow”, respectively. In general, the sample annealed at 500 °C exhibited a similar fast and medium component but significantly increased lifetimes from the slow component, compared to the sample annealed at 350 °C. The normalized amplitudes of these three components provide additional information regarding the origin of these lifetimes. The amplitudes of the fast, medium, and slow



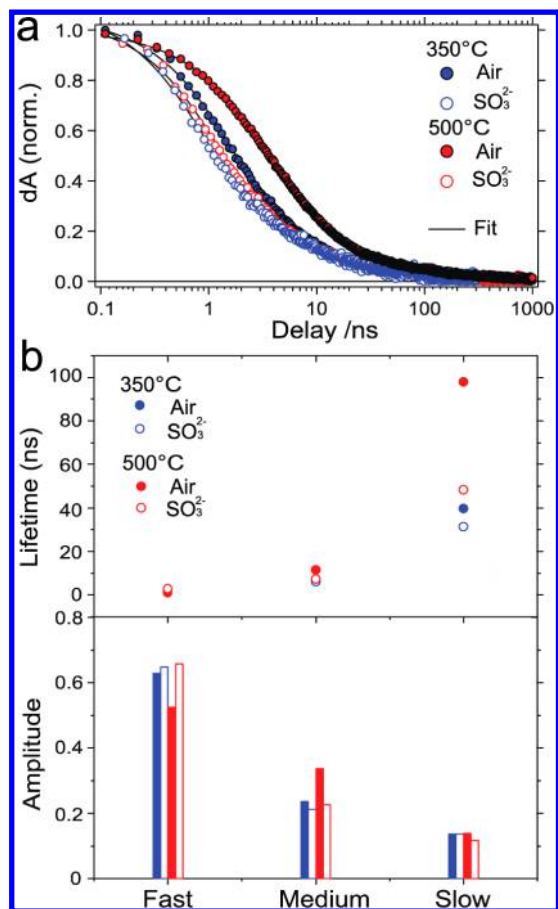


**Figure 3.** (a) Transient absorption decay response (excitation pulse  $\lambda = 350$  nm, transient signal between 450 and 495 nm) of BiVO<sub>4</sub> annealed at 350 and 500 °C collected in air and submerged in 1 M potassium phosphate buffer (pH = 6.8) with 0.1 M Na<sub>2</sub>SO<sub>3</sub>, along with the kinetic model fits using eq S1. (b) Fit parameters showing the extracted lifetimes (top) and the normalized initial amplitudes (bottom) of the fast, medium, and slow components, where  $A_{\text{fast}} + A_{\text{medium}} + A_{\text{slow}} = 1$ . The slow component-stretching factor was 0.5.

components for the samples annealed at 350 °C (500 °C) were 0.63, 0.24, and 0.14 (0.52, 0.34, and 0.14). By increasing the annealing temperature, the amplitude of the fast component decreased relative to that of the medium component, whereas the slow component remained the same. Given the increased crystalline order and grain size observed with 500 °C annealing, we correlate the fast component with rapid carrier recombination at internal defect sites, whose concentrations can be reduced through annealing. At longer times, corresponding to the medium component, a second bulk recombination pathway dominates the observed dynamic relaxation. As the fast recombination channel is eliminated, the relative contribution from the medium component, which appears to be less affected by annealing, increases. Recently, Ravensbergen et al. demonstrated that recombination of trapped carriers occurs between 10 ns and 10  $\mu$ s.<sup>44</sup> As discussed below, we also attribute the slow component observed here to be due to trap state-mediated recombination, in the present case at the surfaces of nanocrystalline BiVO<sub>4</sub>.

To further examine the role of the surface in these samples and correlate the TA dynamics with the PEC performance, samples annealed at 350 and 500 °C were immersed in a 0.1 M sodium sulfite solution (a hole scavenger). In such a solution,

upward band bending of both valence and conduction bands at the semiconductor solution interface is expected. Consequently, electron–hole separation should be increased, with holes preferentially drifting toward the surface in the presence of the electric field below the semiconductor/electrolyte junction.<sup>45,46</sup> While a similar field may exist for the case of BiVO<sub>4</sub> in air, hole transfer to sodium sulfite in solution reduces the instantaneous concentrations of accumulated holes near the surface. The relaxation dynamics of both types of samples, shown in Figure 3a, were accelerated in the electrolyte compared to in air, with lifetimes of 0.9, 6.1, and 30 ns for the sample annealed at 350 °C and 1.1, 7, and 50 ns for the sample annealed at 500 °C, as shown in the top panel of Figure 3b. Consistent with their assignment as bulk recombination pathways, the fast and medium components were only slightly affected by the environment. However, the longer lifetime was significantly reduced by the introduction of an additional recombination route corresponding to the transfer of photoholes to solution. This is especially evident in the sample annealed at 500 °C, where the improved sample quality is likely to have improved the surface and near-surface region of the semiconductor, therefore favoring charge transfer. These results support the conclusion that the surface and near-surface region of the nanostructured BiVO<sub>4</sub> thin films play important roles on recombination dynamics of long-lived excited states. The longer carrier lifetimes, which aid in improving efficiency for driving oxidation reactions in solution, are enabled by the lower defect concentrations and result in increased photocurrent densities, as described below.

To evaluate the PEC performance, the BiVO<sub>4</sub> films annealed at 350 and 500 °C ( $\sim 200$  nm thickness) were prepared as photoelectrodes on FTO glass substrates and the current density–voltage ( $J$ – $E$ ) curves are reported in Figure S11. The photocurrent densities were 0.5 mA cm<sup>-2</sup> and 0.8 mA cm<sup>-2</sup> at 1.23 V vs RHE for the samples annealed at 350 and 500 °C, respectively. The higher photocurrent density measured for the 500 °C sample is consistent with the observation of longer relaxation times and reduced carrier trapping compared with the sample annealed at lower temperature. It is important to note that, while these photocurrent values are lower than state-of-art BiVO<sub>4</sub>-based photoanodes, undoped BiVO<sub>4</sub> is commonly reported with photocurrent densities around 1 mA cm<sup>-2</sup> at 1.23 V vs RHE.<sup>8,47,48</sup>

BiVO<sub>4</sub> has a relatively low majority electron mobility compared to other metal oxide materials.<sup>44–46,49</sup> For bulk BiVO<sub>4</sub> materials, where a larger fraction of the photoelectrons decay through the  $\sim 40$  ns bulk channel, the diffusion lengths remain longer ( $\sim 100$  nm in bulk material).<sup>7,50</sup> Herein, when coupled with the large fraction of short lifetime pathways due to the large surface to volume ratio, the majority carrier diffusion lengths are likely to be decreased and extraction of electrons to the back contact may limit the achievable photocurrent density. This observation provides a strong impetus to couple the nanostructured BiVO<sub>4</sub> light absorber to a secondary nanostructured metal oxide material that possesses improved electron transport properties in order to mitigate the limitations arising from short majority carrier diffusion lengths. If materials possessing appropriate band alignment are utilized, formation of a solid state bulk heterojunction nanocomposite is expected to improve electron charge extraction efficiency and, consequently, overall photoelectrochemical performance.

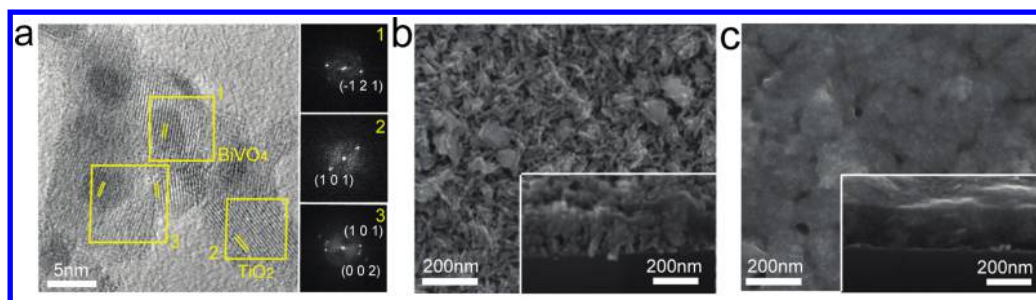


**Figure 4.** (a) HR-TEM image of BiVO<sub>4</sub>/TiO<sub>2</sub>-big nanocomposite, along with the FFTs from the corresponding regions enclosed by labeled yellow boxes (right). (b) and (c) SEM images on the surface and in cross-section (inset) of the BiVO<sub>4</sub>/TiO<sub>2</sub>-big and BiVO<sub>4</sub>/WO<sub>3</sub>-big nanocomposites, respectively.

**Assembly of BiVO<sub>4</sub>/MO Heterostructured Nanocomposites.** To demonstrate and explore the unprecedented tunability afforded by our novel colloidal-based approach to MO heterostructured photoanodes, we have chosen BiVO<sub>4</sub>/WO<sub>3</sub>, BiVO<sub>4</sub>/TiO<sub>2</sub>, and BiVO<sub>4</sub>/Al<sub>2</sub>O<sub>3</sub> bulk heterojunctions as representative examples. Among BiVO<sub>4</sub> heterojunction systems, BiVO<sub>4</sub>/WO<sub>3</sub> has been the most studied system so far, typically in planar thin film form or in nanowire arrays with length in the micron-scale range.<sup>19–27</sup> The band alignment between these two oxides favors electron transfer from the conduction band of BiVO<sub>4</sub> to that of WO<sub>3</sub>, while also preventing hole transfer from the valence band of BiVO<sub>4</sub> to that of WO<sub>3</sub>. Therefore, such heterojunctions promote charge separation and inhibit recombination.<sup>19–27</sup> In contrast, measurements of band positions of bulk TiO<sub>2</sub> and BiVO<sub>4</sub> suggest that the conduction band of TiO<sub>2</sub> lies slightly above that of BiVO<sub>4</sub> in energy; yet, increases of photocurrent density have been recorded from BiVO<sub>4</sub>/TiO<sub>2</sub> nanocomposites when compared to pure BiVO<sub>4</sub>.<sup>17,18</sup> In this case, the transfer of high-energy electrons, photoexcited above the band edge, from the BiVO<sub>4</sub> to the TiO<sub>2</sub> conduction band has been suggested.<sup>17,18</sup> Finally, Al<sub>2</sub>O<sub>3</sub> presents a large energy barrier for transfer of both electrons and holes and no additional charge separation at the interface is expected. Therefore, this materials system represents a valuable reference in the TA measurements that will be described in the following section.

In the present work, we have fabricated BiVO<sub>4</sub>/MO nanocomposites by spin-coating hexane solutions containing the Bi<sub>2</sub>O<sub>2.7</sub>/VO<sub>x</sub> NC heterodimers mixed in different ratios with hexagonal WO<sub>3</sub>, anatase TiO<sub>2</sub>, and Al<sub>2</sub>O<sub>3</sub> NCs of various size and shape (Figure S12). Specifically, WO<sub>3</sub> linear nanorods with two different aspect ratio (5 × 10 nm and 5 × 60 nm, WO<sub>3</sub>-small and WO<sub>3</sub>-big, respectively), TiO<sub>2</sub> linear nanorods (4 × 16 nm, TiO<sub>2</sub>-small) and branched nanorods (TiO<sub>2</sub>-big), and quasi-spherical Al<sub>2</sub>O<sub>3</sub> NCs were examined (see Supporting Information for experimental details). After annealing the heterodimer/MO thin films in air at 500 °C for only 10 min, monoclinic BiVO<sub>4</sub> was formed and the MO morphology was preserved, as evidenced by XRD (Figure S13). No apparent peak shift of the monoclinic BiVO<sub>4</sub>, which would indicate Ti- or W- bulk doping or alloying, was observed in the XRD patterns of the composites.<sup>19</sup> Because of the use of precrystallized building blocks, our annealing time is much shorter compared to other methods.<sup>7,21</sup> To cite one example, 11 hours of annealing at 500 °C was required for the case of the W, Mo-doped BiVO<sub>4</sub>/WO<sub>3</sub> helix nanostructures.<sup>21</sup>

The different processing conditions reported here likely account for the limited interdiffusion of the elements across the BiVO<sub>4</sub>/MO interface and thus explains the absence of high

doping levels that have been observed in previously reported heterostructured architectures. Figure 4a shows a representative HR-TEM image of BiVO<sub>4</sub>/TiO<sub>2</sub>-big nanocomposites, together with selected area FFTs, that reveals the existence of an intimate contact between the TiO<sub>2</sub> and the BiVO<sub>4</sub> domains. SEM images of BiVO<sub>4</sub>/WO<sub>3</sub>-big, BiVO<sub>4</sub>/TiO<sub>2</sub>-big, and BiVO<sub>4</sub>/Al<sub>2</sub>O<sub>3</sub> nanocomposites (50/50 w/w), shown in Figure 4b,c and in the Supporting Information (Figure S14), reveal a uniform distribution of the MO NCs within the BiVO<sub>4</sub> films. In agreement with the XRD data, the initial MO morphology is largely preserved and the BiVO<sub>4</sub> morphology and grain size in the nanocomposites are equivalent to the pure BiVO<sub>4</sub> films (Figure S5). The UV–vis absorption spectra of the nanocomposites reported in Figure S15 revealed a composition-dependent absorption band edge in agreement with previous work.<sup>21,24</sup>

**PEC and TA studies of BiVO<sub>4</sub>/WO<sub>3</sub> heterostructured nanocomposites.** Following the assembly of the BiVO<sub>4</sub>/MO heterojunctions, we utilized these nanocomposites as platforms for understanding the roles of structure and composition on charge separation, transport, and photoelectrochemical performance in bulk heterojunction photoanodes. The conduction band (CB) level of WO<sub>3</sub> lies energetically lower than that of BiVO<sub>4</sub> and photoinduced electron transfer from BiVO<sub>4</sub> to WO<sub>3</sub> should be possible. At the same time, the valence band (VB) level of WO<sub>3</sub> lies significantly lower in energy than that of BiVO<sub>4</sub> and no photoinduced hole transfer is expected.<sup>19–27</sup> Thus, WO<sub>3</sub> should provide an electron selective charge extraction interface. Because of this favorable energetic alignment for selective electron extraction from BiVO<sub>4</sub>, the BiVO<sub>4</sub>/WO<sub>3</sub> materials system is ideal for probing the role of nanocomposite structure on charge separation and transport via PEC and TA measurements. Trends in PEC characteristics and correlations with photocarrier dynamics provide important insights that can guide future developments of such nanocomposites and allow verification of our novel approach. We also note that prior experiments on BiVO<sub>4</sub>/TiO<sub>2</sub> interfaces have suggested the possibility of selective electron transfer, despite the observation that the CB of single crystalline TiO<sub>2</sub> lies ~0.4 eV above the CB of BiVO<sub>4</sub>.<sup>17,18</sup> While preliminary results from our BiVO<sub>4</sub>/TiO<sub>2</sub> nanocomposites also suggest the possibility for selective charge transfer, unravelling potentially nontraditional injection mechanisms, such as hot carrier transfer, within complex metal oxide composites introduces considerable uncertainty in interpretation and will be addressed in a future contribution.

The PEC performance characteristics of the nanocomposites were evaluated by measuring J-E curves and incident-photon-to-current efficiency (IPCE) (Figure 5a,b). Measurements were

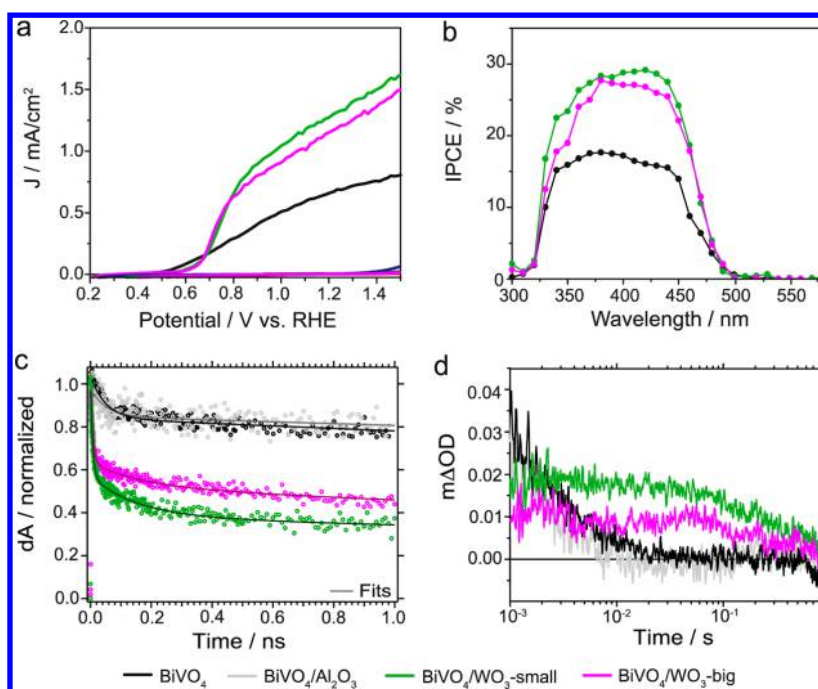


**Figure 5.** (a) Current density vs potential (J-E) curves of photoelectrodes prepared from the different nanocomposites measured under illumination (continuous traces) and in dark (dashed traces) in a 1 M phosphate buffer (pH 6.8) containing 0.1 M  $\text{Na}_2\text{SO}_3$  as hole scavenger and (b) incident photon-to-current efficiency (IPCE) measured at 1.23 V vs RHE. (c) Transient absorption decay response in the ps time scale (excitation pulse  $\lambda = 350$  nm, transient signal probed at 475 nm) of different nanocomposites compared with the pure  $\text{BiVO}_4$  thin film. (d) Transient absorption decay traces of different nanocomposites in the ms time scale (excitation pulse  $\lambda = 355$  nm, transient signal probed at 550 nm).

conducted on samples with 50/50 w/w  $\text{BiVO}_4/\text{WO}_3$  composition under AM 1.5G simulated solar irradiation and in the presence of 0.1 M  $\text{Na}_2\text{SO}_3$  as a hole scavenger. The presence of hole scavenger in solution enables determination of the inherent performance of these thin film light absorbers without convoluting the potentially variable catalytic activities of their surfaces or needing to incorporate, a separate water oxidation catalyst, which is beyond the scope of this work. The J-E curves in Figure 5a show that all  $\text{BiVO}_4/\text{WO}_3$  nanocomposites approximately double the photocurrent density relative to the pure  $\text{BiVO}_4$  film. At 1.23 V vs RHE, photocurrent densities of 0.68, 1.20, and 1.32  $\text{mAcm}^{-2}$  were measured for pure  $\text{BiVO}_4$ ,  $\text{BiVO}_4/\text{WO}_3$ -big, and  $\text{BiVO}_4/\text{WO}_3$ -small, respectively. Thus, an approximately 2 $\times$  enhancement of the current density in the nanocomposites with respect to the pure  $\text{BiVO}_4$  was observed. Moreover, the small  $\text{WO}_3$  nanorods lead to an enhanced charge separation efficiency of 14% compared with the big  $\text{WO}_3$  nanorods (see details in the Supporting Information). In agreement with the J-E curves, the IPCE at 1.23 V vs RHE shows an approximately doubling of efficiency in the nanocomposites, with the highest IPCE values achieved in the  $\text{BiVO}_4/\text{WO}_3$ -small nanocomposites (30% at 430 nm). The result of smaller size  $\text{WO}_3$  outperforming more extended crystals contrasts with previous work on  $\text{BiVO}_4/\text{WO}_3$  heterojunctions where superior PEC performance were achieved by integrating longer  $\text{WO}_3$  nanowires possessing intrinsically improved charge transport properties.<sup>19,21,24</sup> This observation indicates that in our case charge transport in the MO domain is not the main parameter governing the photocurrent in the nanocomposites.

TA spectroscopy was utilized to obtain insight into the excited state dynamics and to elucidate the PEC data. Figure 5c shows representative relaxation dynamics of pure  $\text{BiVO}_4$  compared to  $\text{BiVO}_4/\text{WO}_3$  and  $\text{BiVO}_4/\text{Al}_2\text{O}_3$  heterostructures,

probed above the fundamental bandgap and on the ps time scale. Since  $\text{Al}_2\text{O}_3$  presents a large energy barrier for transfer of both electrons and holes,  $\text{BiVO}_4/\text{Al}_2\text{O}_3$  nanocomposites were used as a reference. Photocarrier relaxation characteristics are found to be nearly identical for pure  $\text{BiVO}_4$  and  $\text{BiVO}_4/\text{Al}_2\text{O}_3$  films (Table S2), consistent with the expectation that no charge transfer should occur at the interface between the semiconductor and the insulator. Furthermore, this reference measurement suggests that processing of  $\text{BiVO}_4/\text{MO}$  nanocomposites does not inherently introduce additional electronically active surface and interface states and does not modify the  $\text{BiVO}_4$  morphology.

In the  $\text{BiVO}_4/\text{WO}_3$  nanocomposites, an additional fast component is observed in the transient excited state response. At the probed energy, just above the bandgap, the signal arises from the photoexcited state of  $\text{BiVO}_4$ . Therefore, additional charge recombination or transfer channels will result in faster relaxation from the excited state and accelerate the decay of the transient signal. In the present case, electron transfer from  $\text{BiVO}_4$  to  $\text{WO}_3$  provides an additional decay channel and results in electron depopulation from the  $\text{BiVO}_4$ . Multiexponential fitting reveals that these fast electron transfer processes are characterized by time constants of  $7 \pm 1$  ps (50 ps for pure  $\text{BiVO}_4$  and  $\text{BiVO}_4/\text{Al}_2\text{O}_3$ ). While there was no significant difference in the observed rate of electron transfer between the  $\text{WO}_3$  small and big samples, the amplitudes of these decay components differed with structure. This component contributed to 35% for  $\text{WO}_3$ -big and 42% for  $\text{WO}_3$ -small. It is worth to noting that the relative difference between these two values (17%) is comparable with the charge separation efficiency extracted by the PEC measurements (14%). This implies that the efficiency of photogenerated electron injection across the heterojunction interface was higher for the case of the smaller  $\text{WO}_3$  nanorods.



While the decay of the photoexcited state of BiVO<sub>4</sub> at the picosecond time scale is observed by probing above its bandgap, the associated electron transfer across the heterojunction interface does not correspond to relaxation to the ground state. Indeed, it is expected that charge transfer across the heterojunction interface will significantly increase photo-carrier lifetimes due to the spatial separation of electrons and holes. It has been previously shown that the transient absorption response of BiVO<sub>4</sub> in the spectral range below its bandgap originates from photoexcited holes in the material.<sup>36</sup> Therefore, to better understand the role of the MO in charge separation efficiency and to probe the influence of the charge separation on long-lived photoholes, which are important for water oxidation, TA spectroscopy was performed in the millisecond to second time scale at a probe wavelength of 550 nm. As shown in Figure 5d, the transient absorption characteristics for the pure BiVO<sub>4</sub> and BiVO<sub>4</sub>/Al<sub>2</sub>O<sub>3</sub> nanocomposites are nearly identical, with decay to the ground state occurring within approximately 10 ms. In stark contrast, a residual transient absorption is still observed after ~1 s in the WO<sub>3</sub>-based nanocomposites, thus indicating the presence of long-lived photoexcited hole states in these heterojunction systems. We note that no transient absorption signal was observed for the WO<sub>3</sub> alone (data not shown). The observation of long-lived photohole-related states can be attributed to the suppression of recombination due to the separation of photogenerated holes and electrons in BiVO<sub>4</sub> and WO<sub>3</sub>, respectively.

TA measurements revealed electron injection from BiVO<sub>4</sub> to WO<sub>3</sub>, which is consistent with the band alignment of the two MOs. Importantly, a higher efficiency of electron injection in the WO<sub>3</sub>-small versus WO<sub>3</sub>-big was observed. These data help to elucidate the higher performance of BiVO<sub>4</sub>/WO<sub>3</sub>-small by indicating that efficient charge separation is key to maximizing the PEC performance; once the electrons are injected into WO<sub>3</sub>, charge transport is sufficiently good to not limit overall performance. Improved efficiency of electron injection, likely deriving from a more extended interfacial area between BiVO<sub>4</sub> and WO<sub>3</sub> in the case of WO<sub>3</sub>-small, is thus the relevant parameter for enhancing the photocurrent in the PEC measurements. Optimization of the interface is expected to largely benefit the overall PEC performance in this class of MO photoanode heterojunctions.

The structural tunability afforded by the NC-based architectures, together with combined PEC and TA measurements, allow for important insights into the relative roles of charge separation at the interface and charge transport in the MO, which can each play crucial roles in nanoscale composites. Future in situ optical studies would be helpful to gain further knowledge about the bias-dependent charge dynamics in these nanocomposite photoanodes.<sup>45,51</sup>

In summary, an in situ seed-mediated growth method for the synthesis of colloidal Bi<sub>2</sub>O<sub>2.7</sub>/VO<sub>x</sub> NC heterodimers has been developed. The as-prepared NCs were dispersible in a colloidal stable solution that was then used as precursor ink for the growth of BiVO<sub>4</sub> films upon annealing. This novel ink-based route to constructing BiVO<sub>4</sub> photoanodes shows unique promise in designing more complex and optimized photoanodes. BiVO<sub>4</sub>/MO nanocomposites were assembled, and the MO domain size, shape, and composition were varied. Studies of excited state dynamics from the picosecond to the second time domain provided insight into charge injection across the BiVO<sub>4</sub>/WO<sub>3</sub> interface, which results in improved PEC

performance by mitigating low majority carrier diffusion lengths in BiVO<sub>4</sub>, while also increasing the photohole lifetime in the nanostructured BiVO<sub>4</sub>. These results highlight the significant potential afforded by assembly of such oxide nanocomposites and unveil relationships between MO properties and PEC performance. In the future, systematic variation of MO compositions and structures is expected to enable tailored interfacial charge transfer and extraction, thereby providing a route to optimization of PEC performance characteristics. While the focus of this initial study was on BiVO<sub>4</sub>/WO<sub>3</sub> nanocomposites, the generality of this facile method for the assembly of preformed building blocks, which avoids tedious growth optimization and long preparation times, will enable access to a wide range of tailored heterojunctions.

## ■ ASSOCIATED CONTENT

### Supporting Information

The Supporting Information is available free of charge on the ACS Publications website at DOI: 10.1021/acs.nanolett.5b03871.

Experimental details, TEM and SEM images, XRD patterns, EDS, XPS and Raman spectra, absorption spectra, Tauc plots, and *J*-*E* curves (PDF)

## ■ AUTHOR INFORMATION

### Corresponding Authors

\*E-mail: [rbuonsanti@lbl.gov](mailto:rbuonsanti@lbl.gov).

\*E-mail: [idsharp@lbl.gov](mailto:idsharp@lbl.gov).

### Present Address

A.L. and R.B. are currently at Department Institut des Sciences et Ingénierie Chimiques Ecole Polytechnique Fédérale de Lausanne (EPFL)-Valais, Switzerland. Future correspondence should be addressed to [raffaella.buonsanti@epfl.ch](mailto:raffaella.buonsanti@epfl.ch).

### Author Contributions

A.L. and R.B. conceived this study. A.L. synthesized and characterized the materials, including their photoelectrochemical behavior. J.K.C., L.H.H., and I.D.S. designed and carried out the carrier dynamics studies. T.M. performed the elemental analysis of the nanocrystals in solution and of films. All authors contributed to write the manuscript.

### Notes

The authors declare no competing financial interest.

## ■ ACKNOWLEDGMENTS

This material is based upon work performed by the Joint Center for Artificial Photosynthesis, a DOE Energy Innovation Hub, supported through the Office of Science of the U.S. Department of Energy under Award Number DE-SC0004993. Work at the Molecular Foundry was supported by the Office of Science, Office of Basic Energy Sciences, of the U.S. Department of Energy under Contract No. DE-AC02-05CH11231. L.H.H. acknowledges financial support from the Alexander von Humboldt Foundation. We thank Dr Ajay Singh for helpful discussions and Prof. Delia J. Milliron for critical reading of the manuscript.

## ■ REFERENCES

- (1) Huang, Y.-H.; Dass, R. I.; Xing, Z.-L.; Goodenough, J. B. *Science* **2006**, *312*, 254–257.
- (2) Llordés, A.; Garcia, G.; Gazquez, J.; Milliron, D. J. *Nature* **2013**, *500*, 323–326.

- (3) Mefford, J. T.; Hardin, W. G.; Dai, S.; Johnston, K. P.; Stevenson, K. J. *Nat. Mater.* **2014**, *13*, 726–732.
- (4) Szot, K.; Speier, W.; Bihlmayer, G.; Waser, R. *Nat. Mater.* **2006**, *5*, 312–320.
- (5) Wu, Y.; Lazic, P.; Hautier, G.; Persson, K.; Ceder, G. *Energy Environ. Sci.* **2013**, *6*, 157–168.
- (6) Woodhouse, M.; Parkinson, B. A. *Chem. Soc. Rev.* **2009**, *38*, 197–210.
- (7) Kim, T. W.; Choi, K.-S. *Science* **2014**, *343*, 990–994.
- (8) Seabold, J. A.; Choi, K.-S. *J. Am. Chem. Soc.* **2012**, *134*, 2186–2193.
- (9) Huang, Z.-F.; Pan, L.; Zou, J.-J.; Zhang, X.; Wang, L. *Nanoscale* **2014**, *6*, 14044–14063.
- (10) Tian, J.; Sang, Y.; Yu, G.; Jiang, H.; Mu, X.; Liu, H. *Adv. Mater.* **2013**, *25*, 5075–5080.
- (11) Cho, I.-S.; Kwak, C. H.; Kim, D. W.; Lee, S.; Hong, K. S. *J. Phys. Chem. C* **2009**, *113*, 10647–10653.
- (12) Hosogi, Y.; Shimodaira, Y.; Kato, H.; Kobayashi, H.; Kudo, A. *Chem. Mater.* **2008**, *20*, 1299–1307.
- (13) Huang, Z.; Lin, Y.; Xiang, X.; Rodríguez-Córdoba, W.; McDonald, K. J.; Hagen, K. S.; Choi, K. S.; Brunshwig, B. S.; Musaev, D. G.; Hill, G. L.; Wang, D.; Lian, T. *Energy Environ. Sci.* **2012**, *5*, 8923–8926.
- (14) Moniz, S. J. A.; Shevlin, S. A.; Martin, D. J.; Guo, J. Z.; Tang, X. *Energy Environ. Sci.* **2015**, *8*, 731–759.
- (15) Li, H.; Zhou, Y.; Tu, W.; Ye, J.; Zou, Z. *Adv. Funct. Mater.* **2015**, *25*, 998–1030.
- (16) Moniz, S. J. A.; Zhu, J.; Tang, J. *Adv. Energy Mater.* **2014**, *4*, 20130590–20130594.
- (17) Xie, M.; Fu, X.; Jing, L.; Luan, P.; Feng, Y.; Fu, H. *Adv. Energy Mater.* **2014**, *4*, 1300995–1300998.
- (18) Ho-Kimura, S.; Moniz, S. J. A.; Handoko, A. D.; Tang, J. *J. Mater. Chem. A* **2014**, *2*, 3948–3953.
- (19) Rao, P. M.; Cai, L.; Liu, C.; Cho, I. S.; Lee, C. H.; Weisse, J. M.; Yang, P.; Zheng, X. *Nano Lett.* **2014**, *14*, 1099–1105.
- (20) Ma, M.; Kim, J. K.; Zhang, K.; Shi, X.; Kim, S. J.; Moon, J. H.; Park, J. H. *Chem. Mater.* **2014**, *26*, 5592–5597.
- (21) Shi, X.; Choi, I. Y.; Zhang, K.; Kwon, J.; Kim, D. Y.; Lee, J. K.; Oh, S. H.; Kim, J. K.; Park, J. H. *Nat. Commun.* **2014**, *5*, 4775–4783.
- (22) Grigioni, I.; Stamplecoskie, K. G.; Selli, E.; Kamat, P. V. *J. Phys. Chem. C* **2015**, *119*, 20792–20800.
- (23) Hong, S. J.; Lee, S.; Jang, J. S.; Lee, J. S. *Energy Environ. Sci.* **2011**, *4*, 1781–1787.
- (24) Su, J.; Guo, L.; Bao, N.; Grimes, C. A. *Nano Lett.* **2011**, *11*, 1928–1933.
- (25) Zhang, K.; Shi, X.-J.; Kim, J. K.; Park, J. H. *Phys. Chem. Chem. Phys.* **2012**, *14*, 11119–11124.
- (26) Pilli, S. K.; Janarthanan, R.; Deutsch, T. G.; Furtak, T. E.; Brown, L. D.; Turner, J. A.; Herring, A. M. *Phys. Chem. Chem. Phys.* **2013**, *15*, 14723–14728.
- (27) Pihosh, Y.; Turkevych, I.; Mawatari, K.; Asai, T.; Hisatomi, T.; Uemura, J.; Tosa, M.; Shimamura, K.; Kubota, J.; Domen, K.; Kitamori, T. *Small* **2014**, *10*, 3692–3699.
- (28) Kovalenko, M. V.; Schaller, R. D.; Jarzab, D.; Loi, M. L.; Talapin, D. V. *J. Am. Chem. Soc.* **2012**, *134*, 2457–2460.
- (29) Murray, C. B.; Kang, Y.; Ye, X.; Chen, J.; Qi, L.; Diaz, R. E.; Doan-Nguyen, V.; Xing, G.; Kagan, C. R.; Li, J.; Gorte, R. J.; Stach, E. A.; Murray, C. B. *J. Am. Chem. Soc.* **2013**, *135*, 1499–1505.
- (30) Wang, R. Y.; Tangirala, R.; Raoux, S.; Jordan-Sweet, J. L.; Milliron, D. J. *Adv. Mater.* **2012**, *24*, 99–103.
- (31) Tangirala, R.; Baker, J. L.; Alivisatos, A. P.; Milliron, D. J. *Angew. Chem., Int. Ed.* **2010**, *49*, 2878–2882.
- (32) Kinder, E.; Moroz, P.; Diederich, G.; Johnson, A.; Kirsanova, M.; Nemchinov, A.; O'Connor, T.; Roth, D.; Zamkov, M. *J. Am. Chem. Soc.* **2011**, *133*, 20488–20499.
- (33) Kovalenko, M. V.; Scheele, M.; Talapin, D. V. *Science* **2009**, *324*, 1417–1420.
- (34) Niederberger, M.; Garnweitner, G.; Pinna, N.; Antonietti, M. *J. Am. Chem. Soc.* **2004**, *126*, 9120–9126.
- (35) Rossell, M. D.; Ramasse, Q. M.; Findlay, S. D.; Rechberger, F.; Erni, R.; Niederberger, M. *ACS Nano* **2012**, *6*, 7077–7083.
- (36) Zhou, H.; Hsu, W.-C.; Duan, H.-S.; Bob, B.; Yang, W.; Song, T.-B.; Hsu, C.-J.; Yang, Y. *Energy Environ. Sci.* **2013**, *6*, 2822–2838.
- (37) Mainz, R.; Singh, A.; Levchenko, S.; Klaus, M.; Genzel, C.; Ryan, K. M.; Unold, T. *Nat. Commun.* **2014**, *5*, 4133–4144.
- (38) Quan, Z.; Luo, Z.; Loc, W. S.; Zhang, J.; Wang, Y.; Yang, K.; Porter, N.; Lin, J.; Wang, H.; Fang, J. *J. Am. Chem. Soc.* **2011**, *133*, 17590–17593.
- (39) Bergerud, A.; Buonsanti, R.; Jordan-Sweet, J. L.; Milliron, D. J. *Chem. Mater.* **2013**, *25*, 3172–3179.
- (40) Paik, T.; Hong, S.-H.; Gauldin, E. A.; Caglayan, H.; Gordon, T. R.; Engheta, N.; Kagan, C. R.; Murray, C. B. *ACS Nano* **2014**, *8*, 797–806.
- (41) Barroso, M.; Cowan, A. J.; Pendlebury, S. R.; Graetzel, M.; Klug, D. R.; Durrant, J. R. *J. Am. Chem. Soc.* **2011**, *133*, 14868–14871.
- (42) Tachibana, Y.; Vayssieres, L.; Durrant, J. R. *Nat. Photonics* **2012**, *6*, 511–518.
- (43) Barroso, M.; Mesa, C. A.; Pendlebury, S. R.; Cowan, A. J.; Hisatomi, T.; Sivula, K.; Gratzel, M.; Klug, D. R.; Durrant, J. R. *Proc. Natl. Acad. Sci. U. S. A.* **2012**, *109*, 15640–15645.
- (44) Ravensbergen, J.; Abdi, F. F.; van Santen, J. H.; Frese, R. N.; Dam, B.; van de Krol, R.; Kennis, J. T. M. *J. Phys. Chem. C* **2014**, *118*, 27793–27800.
- (45) Ma, Y.; Pendlebury, S. R.; Reynal, A.; Le Formal, F.; Durrant, J. R. *Chem. Sci.* **2014**, *5*, 2964–.
- (46) Aiga, N.; Jia, Q.; Watanabe, K.; Kudo, A.; Sugimoto, T.; Matsumoto, Y. *J. Phys. Chem. C* **2013**, *117*, 9881–9886.
- (47) Alarcon-Llano, E.; Chen, L.; Hettick, M.; Mashouf, N.; Lin, Y.; Javey, A.; Ager, J. W. *Phys. Chem. Chem. Phys.* **2014**, *16*, 1651–1657.
- (48) McDonald, K. J.; Choi, K.-S. *Energy Environ. Sci.* **2012**, *5*, 8553–8557.
- (49) Rettie, A. J. E.; Lee, H. C.; Marshall, L. G.; Lin, J.-F.; Capan, C.; Lindemuth, J.; McCloy, J. S.; Zhou, J.; Bard, A. J.; Mullins, C. B. *J. Am. Chem. Soc.* **2013**, *135*, 11389–11396.
- (50) Abdi, F. F.; Han, L.; Smets, A. H. M.; Zeman, M.; Dam, B.; van de Krol, R. *Nat. Commun.* **2013**, *4*, 2145–2152.
- (51) Appavoo, K.; Liu, M.; Black, C. T.; Sfeir, M. Y. *Nano Lett.* **2015**, *15*, 1076–1082.